ELSEVIER

Contents lists available at ScienceDirect

Applied Catalysis A, General

journal homepage: www.elsevier.com/locate/apcata





Catalytic activation of peroxymonosulfate using MnO₂@quasi-MOF for singlet oxygen mediated degradation of organic pollutants in water

Anahita Khojastegi, Amir Mokhtare, Imann Mosleh, Alireza Abbaspourrad

Department of Food Science, College of Agriculture and Life Sciences, Cornell University, Ithaca, NY, USA

ARTICLE INFO

Keywords:
Peroxymonosulfate activation efficiency
Quasi-MOF
Metal leaching inhibition
Water remediation
Heterogeneous catalysis

ABSTRACT

The properties of metal organic frameworks (MOFs), surface area, porosity, and functionality make them an ideal material for heterogenous catalysis. We developed a MnO_2 @quasi-MOF (MnO_2 @q-MOF) catalyst by incorporating MnO_2 into a MIL-53 (Fe) structure with reduction of $KMnO_4$ to MnO_2 followed by a mild heat treatment at 300 °C. MnO_2 @q-MOF showed higher exposed metal sites due to thermally induced decarboxylation and higher activity because of in situ MnO_2 formation while preserving the porosity and crystalline structure of MIL-53 (Fe). We activated potassium peroxymonosulfate (PMS) using our MnO_2 @q-MOF catalyst for decomposition of methylene blue and HEPES in water. The MnO_2 @q-MOF catalyst outperformed both MIL-53 (Fe) and unsupported MnO_2 in the degradation of dye and was reusable. The primary mechanism of PMS activation was revealed to be a singlet oxygen (1O_2) mediated process.

1. Introduction

The safe disposal of industrialized effluents has lagged behind the high rate of upscale material production, which has resulted in massive pollutant discharges into the environment [1]. These industrial effluents often contain high amounts of organic substances, including toxic, non-biodegradable, and recalcitrant compounds, which require immediate action to prevent environmental disturbance [2,3]. Advanced oxidation processes (AOP), typically defined as in situ formation of reactive oxygen species (ROS) for the decomposition of pollutants, offers a possible solution for addressing this issue [2,4,5]. Potassium peroxymonosulfate (PMS) is a robust oxidant that has been increasingly used in sulfate radical-mediated AOPs (SR-AOP) as the primary source of sulfate radical anion ($SO_4^{\bullet-}$), singlet oxygen (1O_2), hydroxyl radical (${}^{\bullet}$ OH), and superoxide radical ($O_2^{\bullet-}$) [6]. The sulfate radicals have high oxidation capabilities, minimum pH dependency, high redox potential, and oxidation selectivity that could replace currently used, yet costly, hydrogen peroxide [7,8]. However, the use of PMS as a reactive oxygen species (ROS) generator requires a transition metal catalysts or high energy activation like thermal or UV radiation [6]. The former activation method, generates nonrecoverable secondary pollutants that may also compromise the water treatment process while the latter (thermal or UV radiation), are not energy efficient and costly [7]. Thus, the development of efficient and reusable heterogeneous catalysts for PMS activation in water is desired [9–11]. New materials such as metal organic frameworks (MOF) can offer a platform to design robust, non-leaching and heterogeneous catalysts for different applications [12, 13]

MOFs are three-dimensional (3D) porous materials that form by the coordination of metal nodes with organic ligands [14,15]. The diversity of available metal nodes and organic linkers make their topological net and 3D structure tunable for various applications through bottom-up fabrication processes [15]. One of the challenges of using MOFs for catalysis is to make uncoordinated metal sites readily available by activation that often requires high temperatures treatment [16]. Once activated, these sites can react with a guest molecule or coordinate with water losing their activity which results in poor catalytic performance [17]. To overcome these problems, MOFs have been functionalized with a secondary metal nanoparticle (NPs) creating a hybrid material [18-20]. In this way, the MOF stabilizes the metal NPs within the confined space of the pores, this prevents aggregation of the high surface energy NPs, as well as reduces metal leaching [21]. The drawbacks of this method are pore blockage and weak interactions between the metal nodes with the guest NPs [22–24]. Alternatively, pyrolysis of organic linkers to expose active metal sites, creating metal oxides from MOF metal nodes, has been shown to boost the catalytic activity [25,26]. There are drawbacks to pyrolysis, however, such as MOF structural collapse caused by extended high-temperature treatments, which results

E-mail address: alireza@cornell.edu (A. Abbaspourrad).

 $^{^{\}ast}$ Corresponding author.

in a decrease in surface area, crystallinity, and porosity [22–24]. Therefore, a synthetic route that retains the MOF structure, and showing metal oxide catalytic activity is highly sought-after.

First reported in 2018, controlled pyrolysis of MOFs has been shown to preserve the high crystallinity, surface area and porosity of the original MOF, while exposing additional active metal sites [22]. This new material, with the hybrid properties of a MOF and metal oxide, is called a quasi-MOF and features exposed metal sites that can interact with metal nanoparticles (NPs) as guest molecules and thus increase catalytic activity [22–24,27,28]. Based on this recent material fabrication method and considering the requirements of aqueous pollutant treatment such as safety, recoverability, and low cost, we synthesized a new type of quasi-MOF catalyst.

In this study, we chose MIL-53 (Fe), a member of the family of Iron (III)-terephthalate MOFs. MIL-53 (Fe) has large 1D pores suitable for encapsulation of NPs and is an excellent source of iron. MIL-53 (Fe) is also stable in boiling water, organic solvents, and in acidic conditions [29,30]. Incorporating Mn into iron-containing MOFs during the initial MOF synthesis has been shown to improve the rate of Fenton reaction for the destruction of tetrachloroethylene and trichloroethylene in water [12]. The combination of Fe and Mn into a single MOF catalyst has been shown to provide a synergistic effect on the activation of PMS [31–33]. However, this improvement comes with the cost of coordinating metal sites with host molecules, and quick catalytic activity loss [18,22,34]. Therefore, to benefit from the presence of Mn and higher activity while addressing the above-mentioned issues, we chose to introduce MnO2 as a secondary site in the structure of our quasi-MOF. Our MnO2@q-MOF catalyst takes advantage of the porosity of the original MOF while providing a platform for stabilizing small particles of MnO2 within the confined space of the pores. We studied our new catalyst, MnO2@q--MOF, for its ability to activate PMS and the impact on the MnO2@q--MOF/PMS system to decompose methylene blue (Mb) and N-2-hydroxyethylpiperazine-N'-2-ethanesuflonic acid (HEPES) as model organic pollutants in aqueous systems.

2. Materials and methods

2.1. Chemicals

All the chemicals, solvents, and reagents were used as received. We used Milli-Q water for all experiments unless otherwise specified. Reagent grade ethanol (EtOH), both absolute, and denatured with 5% methanol, and methanol (99%) were obtained from IBI Scientific, Bioworld, and Fischer chemical, respectively. We purchased the following items from sigma Aldrich (ACS or reagent grade): terephthalic acid (99%), methylene blue (Mb, 95%), acetonitrile (99%, HPLC grade) N, N-dimethylformamide (DMF, 99.9%), iron(III) chloride hexahydrate (FeCl₃0.6 H₂O, 97%), potassium permanganate (KMnO₄, 99%), *tert*-butanol (*t*-BuOH) (99%), 1,4-benzoquinone (BQ), L-histidine (His), 2,2,6,6-tetramethyl-4-piperidone (TEMP, 98%), 4-(2-hydroxyethyl) piperazine-1-ethanesulfonic acid (HEPES, 99.5%), and 5,5-dimethyl-1-pyrroline N-oxide (DMPO, \geq 97%).

2.2. Instrumentation

X-ray photoelectron spectroscopy (XPS) and X-ray powder diffraction (XRD) measurements were obtained on a Scientia Omicron ESCA 2SR machine equipped with an Al K α high power X-ray source and a Bruker D8 Advanced Eco with Cu K α radiation X-ray diffractometer. To study textural and morphological properties of these samples, we used a scanning electron microscopy (SEM) with a Zeiss Gemini 500 microscope and transition electron microscopy (TEM) with a FEI F20 microscope with STEM mode. The FTIR spectrum of the materials were carried out on an IRAffinity-1S (Shimadzu, Japan) equipped with an ATR module. Thermogravimetric analysis (TGA) with a starting temperature of 25 °C under a N2 atmosphere with a heating rate of 10 °C min $^{-1}$ was

carried out on a TA Instruments Q500 Thermogravimetric Analyzer. $\rm N_2$ adsorption-desorption isotherms were collected at 77 K on samples that were degassed and stored under vacuum at 150 $^{\circ} \rm C$ for 24 h using a Micromeritics ASAP 2460 to evaluate porosity and surface area. Subsequently, we obtained specific surface areas, using the modified Brunauer–Emmett–Teller (BET) method.

2.3. Synthesis of MIL-53 (Fe)

MIL-53 (Fe) was synthesized following a previously reported method with some modifications [35]. Specifically, terephthalic acid (1 mmol, 0.206 g) and FeCl₃•6 H₂O (1 mmol, 0.375 g) were added to a Teflon-lined autoclave containing 15 mL of DMF. The autoclave was held at 135 °C for 20 h. After cooling, the reaction mixture was transferred to a centrifuge tube and centrifuged at 12,000 g for 10 min. The orange solid (Fig. 1) was heated and suspended in EtOH, stirred at 65 °C for 2 h, and then filtered. This procedure was performed an additional three times, and the resulting powder was dried in a vacuum oven at 70 °C for 12 h. The characterization of the isolated orange MIL-53 (Fe) powder matched literature values [36].

2.4. Synthesis of MnO₂@q-MOF

To 250 mL of aqueous KMnO₄ solutions, concentrations ranging from 5 to 100 mg/L, was added 10 mL of 1 M $\rm H_2SO_4$. The MIL-53 (Fe) (0.1 g) was dispersed in the KMnO₄ solution by sonication for 30 min. The mixture was stirred for 2 h at 60 °C, transferred to a centrifuge tube and centrifuged (12,000 g for 10 min), then the pellet was washed with EtOH and water approximately ten times, and decanted. The resulting light brown powder (Fig. 1) was dried at 60 °C for 2 h and was heated at 300 °C under a flow of N₂ for 2 h to obtain MnO₂@q-MOF.

2.5. Degradation of Mb and HEPES using MnO₂@q-MOF/PMS

Degradation conditions were varied to explore the effects of different concentrations, temperatures, pH levels and added ions. The condition for the optimized catalytic system is as follows: Into a 500 mL beaker was added 300 mL of a 50 mg/L aqueous solution of organic pollutant, followed by 0.2 g/L of the MnO2@q-MOF. Using 0.1 M NaOH or 0.1 M $\rm H_2SO_4$ solution, the pH of the mixture was adjusted to 7. After allowing sufficient time (30 min) for the catalyst to be adequately dispersed, 0.18 g PMS was added to achieve a final concentration of 2 mM. To monitor the kinetics of dye degradation, we withdrew 0.5 mL of the reaction mixture at pre-arranged time intervals and passed them through a 0.22 mm polyvinylidene fluoride mesh membrane to separate the catalyst. To these samples, ethanol (0.5 mL) was instantly injected to quench radicals prior to filtration.

We selected Mb and HEPES as model organic pollutants to study the $MnO_2@q-MOF/PMS$ system. Mb was selected for system optimization because it can be monitored using UV/Vis. Using a SHIMADZU UV/Vis spectrophotometer (UV-2550), we were able to monitor the degradation kinetics of Mb at a maximum wavelength of 664 nm. HEPES was selected as a widely used buffer in the pharmaceutical industry to show the generalized applicability of this catalytic system; the degradation kinetics for HEPES were studied by LC-MS/MS.

An LC-MS/MS (Thermo Q Exactive) ion trap with electrospray ionization in a positive mode was used to determine the degradation intermediates of both Mb and HEPES. Specifically, a reversed-phase C18 (Luna Phenomenex 5 μ M 4.6 $\times 100$ mm) column was used for separation at room temperature. HEPES degradation intermediates were detected with an isocratic elution of 10% acetonitrile and 90% water containing 0.1% formic acid for 15 min with a flow rate of 0.4 mL/min. Mb intermediates were detected by an isocratic elution (75% methanol and 25% of a 20 mM ammonium formate solution in water) for 15 min and a flow rate of 0.4 mL/min.



Fig. 1. A photographic representation of the catalyst synthesis.

2.6. Kinetic study of Mb decomposition

A pseudo-first-order kinetic model was used to describe Mb decomposition using the MnO₂@q-MOF/PMS system:

$$ln\frac{C_t}{C_0} = -k_{app}t$$

Where C_0 and C_t (mg/L) are the initial and the concentration at time t, respectively, $k_{\rm app}$ is the apparent rate constant, and t is reaction time. We evaluated the impacts of different catalyst dosages (0.05–0.20 g/L), the pH level (3–9), reaction temperatures (25–45 °C), and PMS dosages (1–4 mM) on the kinetics of Mb degradation. Multiple coexisting anions (NaCl, NaSO₄ NaH₂PO₄, NaHCO₃) were also added to the reaction system to assess their effects on degradation rate. Several radical scavengers were investigated, including EtOH, His, t-BuOH, and BQ to quench radicals in the reaction system. Utilizing DMPO and TEMP as spin trapping reagents, we detected ROS by electron paramagnetic resonance (EPR) spectroscopy. Concentrations of leached iron and manganese were quantified using inductively coupled plasma/mass spectroscopy (ICP/MS). To demonstrate the reusability of the catalyst, after each run

the catalyst was filtered, rinsed with copious amounts of a 50:50 mixture of EtOH and water, and dried at 60 $^{\circ}\text{C}.$

3. Results and discussion

3.1. Characterization of MnO₂@q-MOF

To synthesize $MnO_2@q$ -MOF, there were three key steps; synthesis of MIL-53 (Fe), in situ generation of MnO_2 in MIL-53 (Fe) structure using $KMnO_4$ solution and controlled thermal treatment under nitrogen to expose the Fe nodes and producing Fe-O to enable their interaction with the guest MnO_2 inside the pores (Fig. 1) [22]. We found out that the presence of Fe-O on the catalyst promotes adsorption of hydroxyl groups on the body of the catalyst and is crucial for PMS activation [31].

3.1.1. XRD pattern of MnO₂@q-MOF

The XRD pattern of MIL-53 (Fe) has several sharp peaks at 20 (degree)= 8.8, 10.6, 15.2, 17.4, and 20.54, indicative of the high crystallinity of the sample (Fig. 2a) which is consistent with previously reported results [30] and that were in good agreement with the simulated

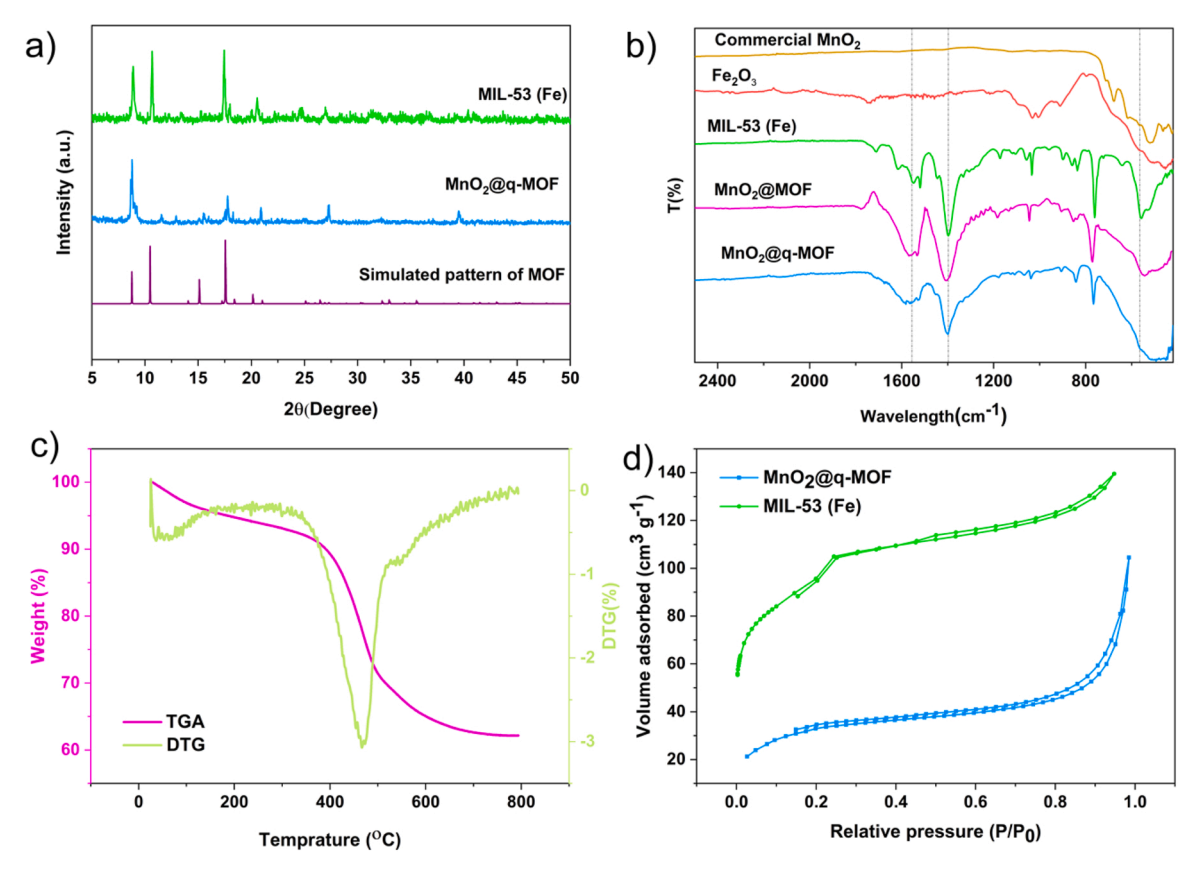


Fig. 2. a) XRD of patten of MIL-53 (Fe), $MnO_2@q$ -MOF and the simulated pattern of MOF acquired from The Cambridge Crystallographic Data Center (CCDC), b) FTIR of commercial MnO_2 , Fe_2O_3 , MIL-53 (Fe), $MnO_2@MOF$ (before thermal treatment), and $MnO_2@q$ -MOF, c) TGA analysis of $MnO_2@q$ -MOF (before thermal treatment), and d) N_2 adsorption-desorption of MIL-53 (Fe) and $MnO_2@q$ -MOF.

pattern. After introducing KMnO₄ and its subsequent reduction to MnO₂, the intensity of most of the peaks decreased, but the quasi-MOF still retained a crystalline structure which suggested that post-synthesis treatments could be considered mild. Specifically, the peak around 2θ= 8.8 showed broadening, which could be attributed to the decarboxylation of MIL-53 (Fe) [22-24,27]. The peak at 2θ = 10.6° disappeared from the spectra, which could be correlated to the breathing effect of MIL-53 (Fe) upon pore filling with MnO₂ and the consequential altering of the unit cell parameters, c and b [37]. In the spectra of MnO2@q-MOF, we did not find any peaks associated with MnO2, revealing the amorphous nature of the encapsulated MnO2 as it has added to the MIL-53 (Fe) framework. The observed changes in the XRD spectra indicate that the amorphous MnO2 nanoparticles were incorporated into the pores of the MIL-53 (Fe) [22,23]. Additionally, we observed a broadening of the peaks in the XRD with increasing the concentration KMnO₄ (Fig. S1) which could be correlated to the increasing the amount of amorphous phase of MnO2 in the crystalline MIL-53 (Fe) framework [38].

3.1.2. FTIR of MnO₂@q-MOF

FTIR was used to identify the functional groups of MnO₂@q-MOF before and after modifications. The MIL-53 (Fe) spectra showed asymmetric and symmetric stretching of the carboxyl group (COO⁻) embedded in the body of the MIL-53 (Fe), at 1395 and 1550 cm⁻¹ (Fig. 2b). The band around 560 cm⁻¹ is associated with the Fe-O bond of the metal cluster. The sharp bands in the FTIR of MIL-53 (Fe) indicate an ordered and defined structure for the MOF [39]. When MIL-53 (Fe) was treated with the KMnO₄, broadening of the carboxylic acid bands at 1395 and 1550 cm⁻¹ was observed. This broadening was attributed to the sensitivity of FTIR to the electromagnetic environment, suggesting the presence of MnO₂ in the structure [39]. We also assigned the broad band in the 400–550 cm⁻¹ area to Mn-O and Fe-O stretching vibrations. After the controlled pyrolysis, we correlated the decline in the intensity and the broadening of the bands at 1395 and 1550 cm⁻¹ to the partial decarboxylation of the MIL-53 (Fe) and carbon dioxide release from the structure, which suggest exposure of metal nodes [22,23].

3.1.3. TGA of MnO₂@MOF

To determine the best temperature for partial decarboxylation and deligandation of the $MnO_2@MOF$ (MIL-53 (Fe) treated with $KMnO_4$ prior to pyrolysis), we used TGA to find the point at which we could expose metal sites without complete structural collapse. The weight loss during thermal treatment of $MnO_2@MOF$ could be categorized into two temperature stages: one around 150 °C and the other above 380 °C (Fig. 2c). We assigned the weight loss at 150 °C to the water evaporation, accounting for almost 5 wt% of the total sample. The significant weight loss between 380 °C and 500 °C is due to decarboxylation and deligandation with an additional weight loss of 25 wt% of the total sample. Based on the TGA results and previous reports, we selected 300 °C as the optimum temperature for thermal treatment of the $MnO_2@MOF$. This temperature is sufficient to modify the MIL-53 (Fe) crystalline structure without complete destruction [22–24].

3.1.4. N_2 adsorption-desorption isotherms of $MnO_2@q\text{-MOF}$

We investigated the impact of the incorporated MnO_2 and the subsequent pyrolysis on pore volume and specific surface area of MIL-53 (Fe) and MnO_2 @q-MOF using N_2 adsorption-desorption isotherms (Fig. 2d). The initial BET surface area of 346.9 m^2/g for MIL-53 (Fe) decreased to $108.5~m^2/g$ for MnO_2 @q-MOF. Similarly, the measured pore volume of $0.135~cm^3/g$ for MIL-53 (Fe) decreased to $0.119~cm^3/g$ for MnO_2 @q-MOF (Table S1), suggesting that the pores of the MIL-53 (Fe) framework may be occupied by MnO_2 and/or blocked by some of the larger particles [40]. Nevertheless, the calculated surface area for MnO_2 @q-MOF is two to two hundred times greater than both previously reported manganese oxide and Fe-Mn paired catalysts [31,32,41], which is a significant finding since the surface area plays a crucial role in

catalytic performance [42].

3.1.5. SEM images of MnO₂@q-MOF

SEM was used to explore the morphology and structure of MnO₂@q-MOF. The SEM images of MIL-53 (Fe) showed perfect hexagonal bipyramidal morphologies varying from 500 nm to 5 mm in size, which agrees well with previous reports (Fig. 3a(i-iii)) [13,36]. SEM images of MnO₂@q-MOF revealed a similar crystalline structure to the MIL-53 (Fe) indicating the mild nature of the pyrolysis treatment (Fig. 3b (i-iii)), however, the crystals of the MnO₂@q-MOF are elongated along one axis with respect to MIL-53 (Fe), indicating both the flexible nature of the lattice and the resulting structural changes caused by the incorporation of MnO₂ and pyrolysis [37,43,44]. Further, the smooth surface of MnO₂@q-MOF particles implies that the main growth of MnO₂ particles occurred inside the pores rather than on the lattice surface [45,46].

Elemental mapping of the $MnO_2@q\text{-}MOF$ obtained from the energy dispersive X-ray (EDX) mode indicate that C, Fe, and O are uniformly distributed throughout the quasi-MOF, but Mn distribution varies based on the particles' size (Fig. 3e). For larger particles, it is predominately found on the outer shell of the catalyst with decreasing distribution toward the core. In smaller particles, it appears to be distributed evenly. The coexistence of C and O in the catalyst emphasizes that the phthalate linkers are still present in the catalyst after thermal treatment.

3.1.6. TEM analysis of MnO₂@q-MOF

TEM images of MIL-53 (Fe) and $MnO_2@q$ -MOF revealed the bipyramidal morphology of the parent MOF (Fig. 3c(i-iii)) which agreed with the SEM results; the surface of the crystals is smooth, and the dark color of the crystals indicates that the MOF crystals are densely packed. After pyrolysis, the crystalline shape of the parent MOF is retained, while the edges and surfaces appear rough (Fig. 3d(i-iii)). The $MnO_2@q$ -MOF particles are also brighter and less dense, implying that the partial loss of phthalate linkers from the parent MOF has reduced packing density, indicating decarboxylation of MOF while retaining the crystalline structure and the successful synthesis of a quasi-MOF [23,27]. The dark spots are indicative of iron and manganese oxide formation and exposed metal sites [27].

3.1.7. XPS analysis of MnO₂@q-MOF

The survey XPS spectrum of MIL-53 (Fe), indicates the existence of Fe, O, and C with the peaks at binding energy (BE) around 710, 529, and 284 eV, respectively (Fig. 4a). The survey XPS spectra of $MnO_2@q\text{-}MOF$ not only shows the same peaks associated with Fe, O, and C, but also indicates a new peak around 641 eV that proves the presence of Mn in the catalyst after introducing MnO_2 and the subsequent thermal treatment, which are in good agreement with the mapping analysis results [33]. Due to the surface-based nature of XPS, we carried out ICP/MS analysis to estimate the amount of Fe and Mn contained in $MnO_2@q\text{-}MOF$, which detected 43.1 mg/g of Mn and 216.3 mg/g of Fe using acid digestion.

High-resolution XPS of MIL-53 (Fe) and MnO2@q-MOF to confirm that the crystallinity of the MIL-53 (Fe) lattice is preserved, and partial decarboxylation and deligandation occurred after the thermal treatment (Fig. 7). The high-resolution XPS spectra of C 1 s of MOF and MnO₂@q-MOF has peaks at 283.85, 285.13, and 288.52 eV which correspond to C-C=H, C-C=C, and O-C=O bonds, respectively (Fig. S2a and c). The existence of the same peaks after MIL-53 (Fe) modification indicates the retention of the phthalate linkers after thermal treatment. The highresolution XPS spectra of O 1 s MIL-53 (Fe) where Peaks at 532.9, 532.1, and 531.1 eV were observed in the high resolution XPS spectra of O 1 s MIL-53 (Fe) and correspond to C=O, C-O, and Fe-O bonds, respectively (Fig. S2b). Peaks at 532.9, 532.1 eV related to the C=O and C-O bond and at 531.6 and 530.03 eV correspond to Fe-O and Mn-O bonds, respectively (Fig. S2d). The decrease in the intensity ratio of the carbon-oxygen bonds to metal-oxygen bonds in MnO2@q-MOF clearly implies the incorporation of MnO2, and partial decarboxylation and

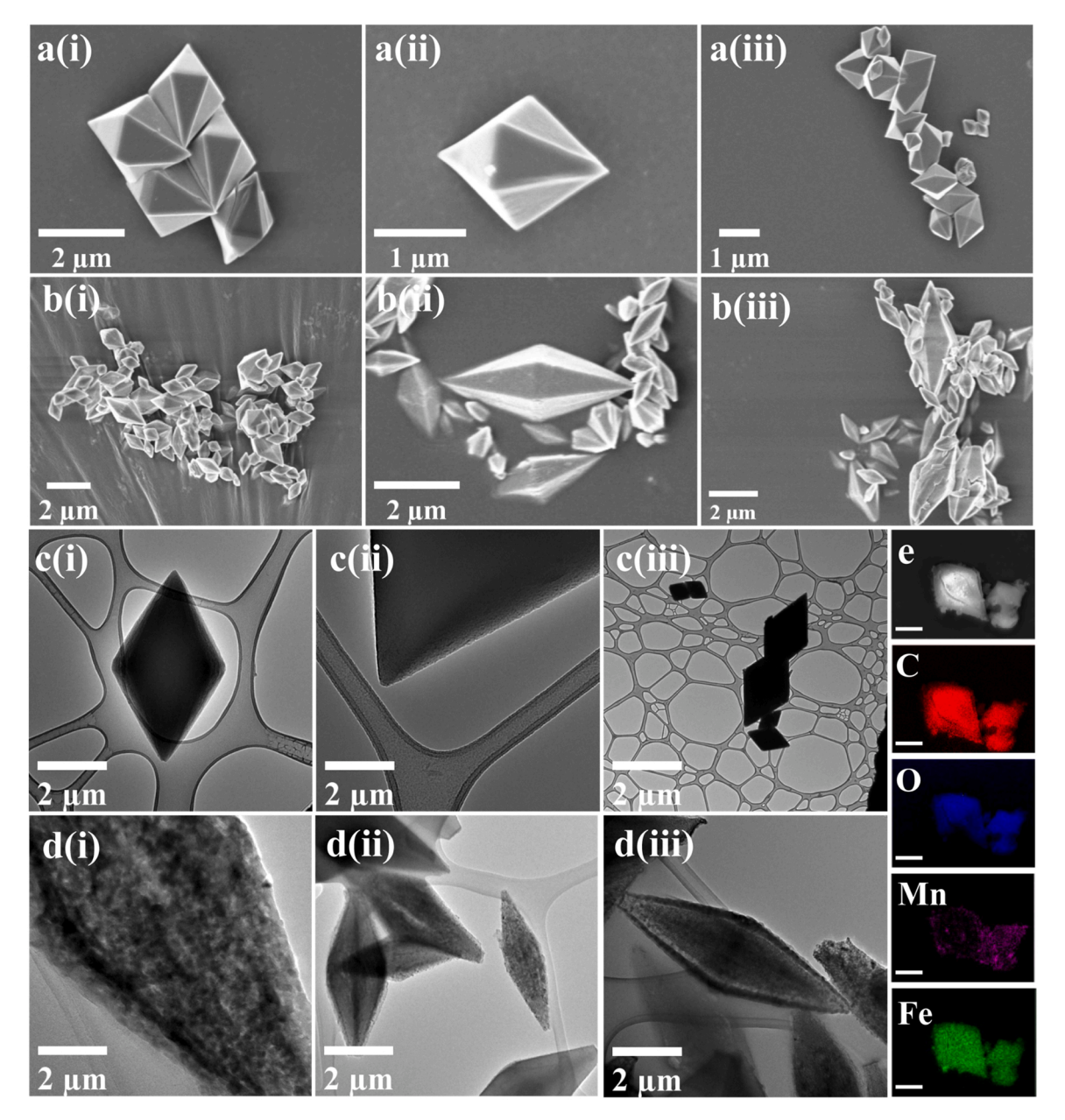


Fig. 3. SEM images of a(i), (ii) and (iii) MIL-53 (Fe), b(i), (ii) and (iii) MnO₂@q-MOF and TEM images of C(i), (ii) and (iii) MIL-53 (Fe), d(i), (ii) and (iii) MnO₂@q-MOF e) elemental mapping of MnO₂@q-MOF for carbon, oxygen, manganese, and iron (scale bar: $2 \mu m$).

deligandation of MIL-53 (Fe) framework [33].

The Fe 2p spectra consist of two peaks related to the spin-orbit splitting of Fe $2p_{3/2}$ and Fe $2p_{1/2}$ (Fig. 4b). Fe(III) shows characteristic peaks around 725 and 711 eV with a shake-up peak at 719 eV, and Fe(II) shows peaks at 723 and 709 eV with a shake-up peak at 715 eV [13,36]. The higher BE peak around 713 eV indicates an interaction between Fe (III) and Fe(II). Further, the decreased intensity ratio of Fe(II):Fe(III) from 0.24 to 0.21 in the deconvoluted Fe 2p spectrum of MIL-53 (Fe) and MnO₂@q-MOF indicate oxidation of Fe(II) by KMnO₄ after the chemical modification of the MIL-53 (Fe) [12,36].

A characteristic spin—orbit doublet of Mn $2p_{3/2}$ and Mn $2p_{1/2}$ in the Mn 2p spectra, where the two are distanced by 11.9 ± 0.1 eV was observed (Fig. 4d). Mn $2p_{3/2}$ peak is further resolved into four peaks with BE at 645.6, 642.5, 641.3, and 640.0 eV corresponding to the shake-up signal, Mn(IV), Mn(III), and Mn(II), respectively [33]. These results indicate that MnO $_2$ presence is in the form of Mn (IV), Mn (III), and Mn (II) with different ratios.

3.2. Catalytic performance of MnO₂@q-MOF

We investigated the catalytic performance of $MnO_2@q-MOF$ toward PMS activation and the degradation of Mb with various ratios of MnO_2 , catalyst, PMS dosages, different pH levels, and temperatures (Fig. 5).

3.2.1. Effect of MOF modification on catalytic activity and its comparison to individual components on Mb removal

The degradation rate of Mb using $MnO_2@q$ -MOF/PMS system can be best described by a pseudo-first-order kinetic model, and the system achieved more than 97% of Mb degradation within 80 min (Fig. 5a). In contrast, $MnO_2@q$ -MOF and PMS alone achieved less than 5% and 30% of Mb degradation, respectively. These results show that $MnO_2@q$ -MOF alone has a negligible impact on Mb adsorption and decolorization without introducing PMS to the system (Fig. 5a). PMS alone also did not completely oxidize the dye, underlining the role of the catalyst in activating PMS. Further, results indicated that the MIL-53 (Fe) also had low catalytic activity toward the activation of PMS, where only 20% of the

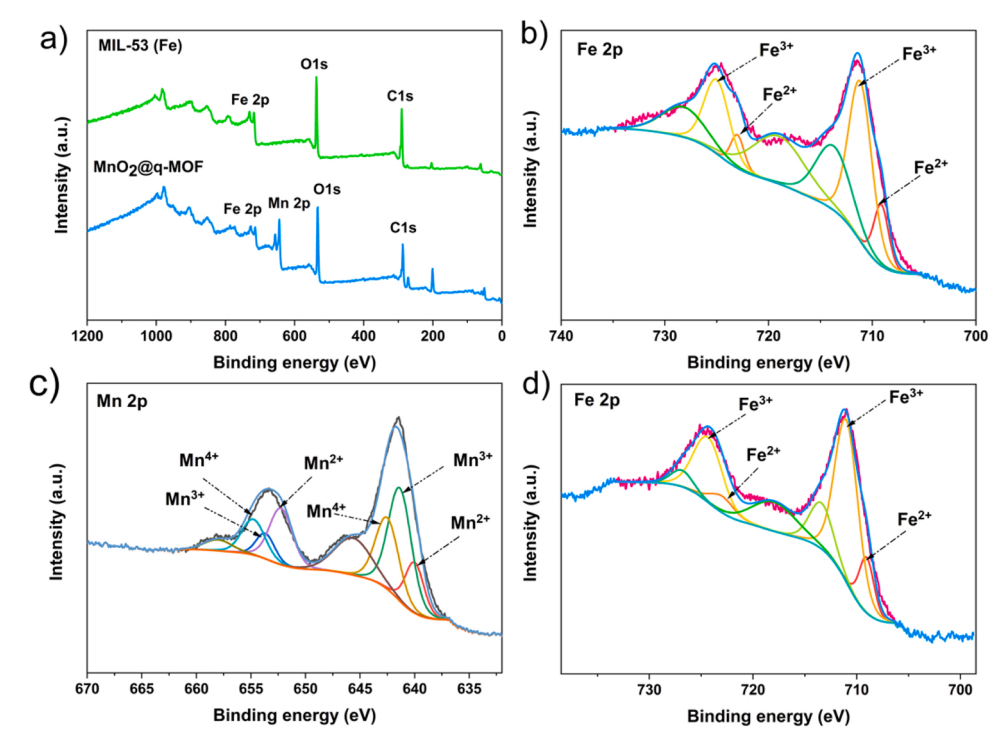


Fig. 4. a) XPS survey spectra, high-resolution spectra of b) Fe 2p of MIL-53 (Fe), c) Mn 2p of MnO₂@q-MOF, and d) Fe 2p of MnO₂@q-MOF.

dye was degraded within 80 min of the reaction suggesting not only poor redox properties of Fe (III)/Fe (II) in the nodes MIL-53 (Fe) and emphasizing the role of the Mn in this catalyst.

Last, we used MnO $_2$ alone as a catalyst (the detailed characterization is provided in SI, Fig. S3) for PMS activation and showed that this system only achieved 50% degradation of Mb within 80 min. This higher degradation level relative to the MIL-53 (Fe)/PMS system is due to MnO $_2$ activity. The inferior performance of MnO $_2$ alone, as compared to MnO $_2$ @q-MOF/PMS system, shows the higher catalytic activity of nanosized MnO $_2$ encapsulated within the MIL-53 (Fe) framework. This also highlights the function of the exposed Fe sites in the catalyst and the possible synergistic effect between the MnO $_2$ nanoparticles and the Fe [12,31,47].

3.2.2. Effect of MnO2 concentration in MnO2@q-MOF

We explored the effect of MnO₂ ratios in the Mb degradation reaction by changing the KMnO₄ concentrations in the synthesis of MnO₂@q-MOF. As shown in Fig. 5b, by changing KMnO₄ concentration from 5 to 15 mg/L, the reaction rate constant (k_{app}) improved from 0.0029 to 0.0122 min⁻¹, showing a 90% improvement, and emphasizing the role of MnO2 in the MnO2@q-MOF activity. Further, increasing the concentration from 15 to 50 mg/L changed the rate constant (k_{app}) from 0.0122 to 0.0322 min⁻¹, demonstrating a 30% improvement in the reaction kinetics (Table S2). However, increasing the KMnO4 concentration to 100 mg/L decreased the rate constant (k_{app}) to 0.0196 min⁻¹. This decrease in reaction rate (k_{app}) constant suggests that 50 mg/L concentration of KMnO₄ is the optimum concentration which provided sufficient activation sites but did not reduce the surface area dramatically. We concluded that the surface area was compromised when more than 50 mg/L KMnO₄ was used in catalyst preparation, resulting in decreased catalytic activity [33,48,49]. Therefore, we chose the catalyst synthesized with 50 mg/L concentration of KMnO₄ as the optimum catalyst for the rest of our studies as it performed most efficiently in removing Mb.

3.2.3. Effect of MnO₂@q-MOF dosage

As it is shown in Fig. 5c and tabulated in Table S2, increasing the catalyst dosage from 0.05~g/L to 0.2~g/L markedly improved the

reaction rate constant (k_{qpp}) by 55% (0.0141–0.0322 min⁻¹), indicating the essential role of the catalyst dosage in the degradation kinetics. Results show that 0.05 g/L of MnO₂@q-MOF is sufficient to degrade Mb up to 95.7% within 120 min, while 0.2 g/L of MnO₂@q-MOF reached 100% degradation within 120 min. Further increasing the catalyst dosage provides more reaction sites for the PMS activation leading to more ROS generation. As such, we chose 0.2 g/L of MnO₂@q-MOF as the optimum value for carrying out the rest of the studies since the highest reaction rate constant (k_{qpp}) was recorded at this concentration (Table S2). Finally, the PMS and catalyst dosages should be adjusted to a proper ratio to maintain maximum efficacy [6].

3.2.4. Effect of PMS dosage

Fig. 5d displays the impact of PMS dosage with the optimum amount of the catalyst (0.2 g/L) on Mb removal. The reaction rate constant (k_{app}) of Mb degradation with 1, 2, and 4 mM of PMS was found to be 0.0173, 0.0321, and 0.0242 min⁻¹, respectively (Table S2). Results showed that fewer ROS are produced at lower concentrations of PMS, resulting in a slower reaction rate. In contrast, at the highest concentrations of PMS, excessive production of ROS leads to a self-quenching phenomenon [6]. Further, it has also been reported that PMS competes with Mb for adsorption sites on catalysts, and its excessive amount can slow down the reaction [50]. Therefore, we found the optimum amount of PMS for Mb degradation to be 2 mM. The reaction rate constant (k_{app}) does not change linearly with respect to PMS dosage, meaning that PMS concentration does not play a role in the reaction kinetic equation and confirming the pseudo first order reaction rate.

3.2.5. Effect of pH

To elucidate the role of pH on the degradation of Mb, first, we conducted an adsorption study before adding PMS to the system. The Mb adsorption is less than 1% for pH 3, 5, and 7 but at pH 9 the material absorbed 9.3% of the Mb and equilibrium adsorption (q_e) was 23.3 mg/g after 30 min (Table S3). This trend was predicted considering the pH of zero charge (pH_{pzc}) for the material is 7.6. At pH 9, the material surface is negatively charged, and thus, can interact with Mb electrostatically. We also investigated the effect of pH on the degradation efficiency of Mb

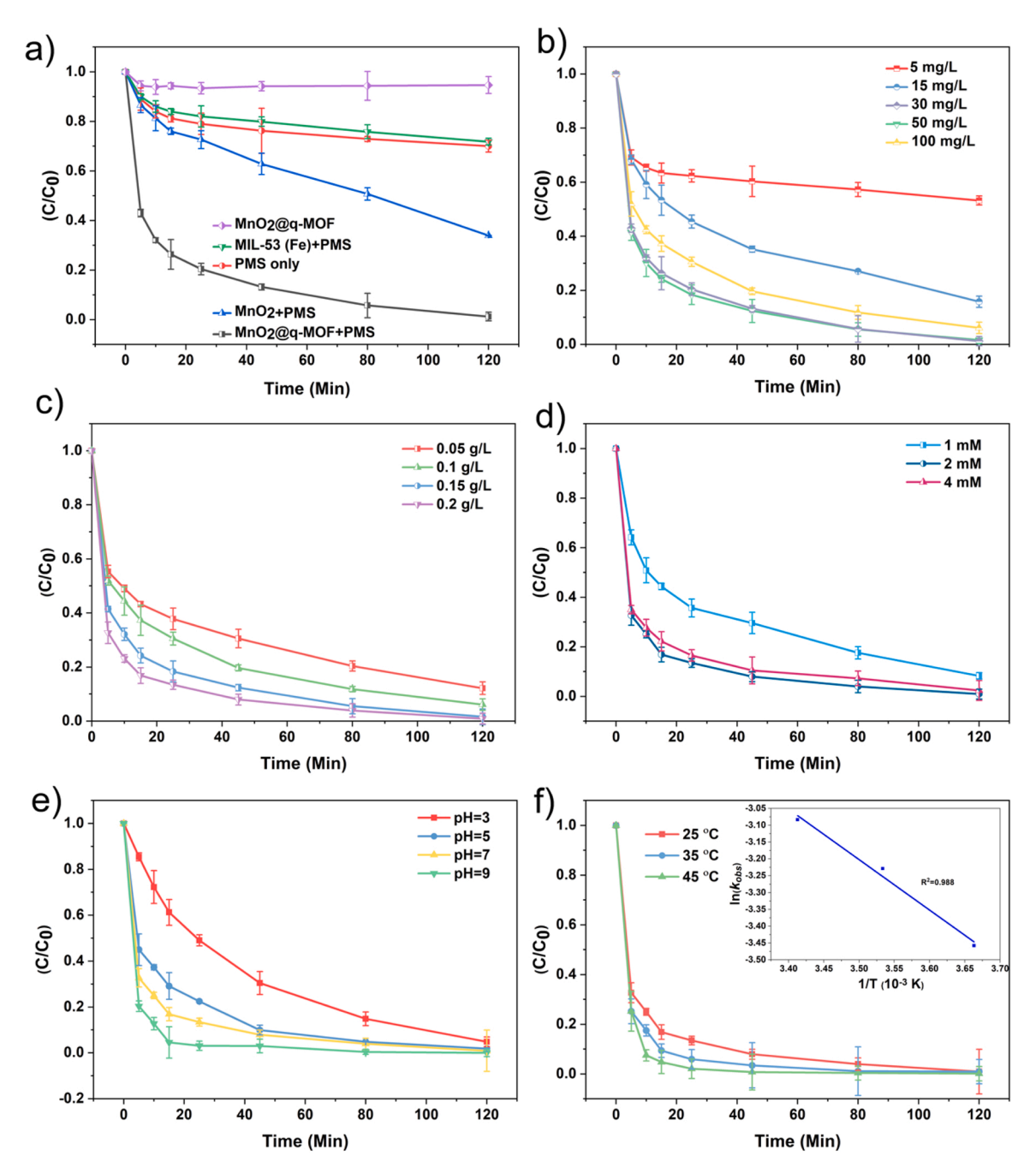


Fig. 5. The decomposition kinetic of Mb a) in different reaction systems, Degradation condition: [Mb]= 50 mg/L, [PMS]= 2 mM, [Catalyst]= 0.15 g/L, b) different loading of MnO₂, Degradation condition: [Mb]= 50 mg/L, [PMS]= 2 mM, [MnO₂ @q-MOF]= 0.15 g/L, c) catalyst dosage, Degradation condition: [Mb]= 50 mg/L, [PMS]= 2 mM, [MnO₂ @q-MOF]= 0.2 g/L, e) effect of pH, Degradation condition: [Mb]= 50 mg/L, [PMS]= 2 mM, [MnO₂ @q-MOF]= 0.15 g/L, and f) effect of temperature, Degradation condition: [Mb]= 50 mg/L, [PMS]= 2 mM, [MnO₂ @q-MOF]= 0.15 g/L, inset graph is the thermodynamic fitting curve of activation energy.

due to the pH-dependent activity of PMS [6]. We performed the degradation reaction at four different pH levels of 3, 5, 7, and 9, and monitored the reaction kinetics (Fig. 5e). Increasing the pH from 3 to 9 improved the degradation of Mb, with an observed increase in the rate constant (k_{app}) of 43% (0.0254–0.0449 min⁻¹). At lower pH levels of 3 and 5, the poor degradation efficiency can be attributed to two phenomena. First, hydronium ions can protonate the peroxide bond of HSO $_{5}^{-}$ inhibiting the activation of PMS by active sites of the catalyst. Second, hydronium ions serve as scavengers for ROS, reducing the degradation efficiency. At higher pH levels, however, it is easier to generate metal-OH species, which are important for the PMS adsorption on the surface of catalysts, resulting in reaction rate acceleration [31].

3.2.6. Effect of temperature

As shown in Fig. 5f, the temperature expectedly had a profound impact on the Mb degradation kinetics. Our results showed that increasing the temperature from 25° to 35°C halved the reaction time to degrade 96% of Mb, and the rate constant (k_{app}) increased from 0.0322 to 0.0369 min⁻¹. Further increase of temperature to 45 °C completely degraded Mb in less than 20 min, and the rate constant (k_{app}) reached 0.0458 min⁻¹, revealing an endothermic nature to the degradation reaction [12]. The reaction rate increase with temperature can be attributed to thermal activation of PMS, and more production of ROS in a shorter reaction time [12]. The inset graph in Fig. 5f shows the thermodynamic fitting curve obtained from Arrhenius's equation [51].

Based on the thermodynamic fitting curve obtained from this equation, the activation energy is calculated, 12.4 kJ/mol which is within the range of some previous reports [12].

3.3. MnO₂@q-MOF stability and reusability

We evaluated the catalyst stability based on leached metal levels detected using ICP/MS analysis. Based on Pearson soft/hard acid-base theory, metal nodes and ligands in a MOF structure can be considered Lewis acids and Lewis bases, respectively [52]. Based on this theory, MOFs with a combination of high valence metals (hard acid) and oxygen terminated ligands (soft base) are resistive to metal leaching and dissolving in acidic and neutral pH, while low valence metals (soft acid) and nitrogen terminated ligands (hard base) are more stable in alkaline and neutral pH [53]. Accordingly, based on the elements present in MIL-53 (Fe), we expect it to be more stable in an acidic and neutral environment. We compared the ICP/MS detected metal ion levels at the different pH levels, which clearly indicated the low amount of leached metal ions at acidic and neutral pH levels (Table S4). The leached metal ions detected in our system are 0.678 mg/L for Fe and 0.504 mg/L for Mn at neutral pH, which are considerably lower than the metal ion leaching in some previous reports [54,55]. In basic conditions, pH 9. however, leached Fe and Mn are 7.069 mg/L and 0.799 mg/L, respectively, considerably higher than acidic and neutral conditions. At pH 9, iron starts to leach out as Fe (III) from the metal nodes of the MIL-53 (Fe) since hydroxide ions can participate in a ligand exchange reaction with terephthalic acid. This is a known drawback of MOFs; they cannot be used over a wide range of pH levels due to metal ion loss through ligand exchange reactions. Although Mn leaching at pH 9 still follows the same trend as other pH levels, it is slightly higher which can be correlated to the exposure of small MnO₂ NPs stabilized and encapsulated within the pores of the MIL-53 (Fe) framework upon leaching of iron [56]. Since the surface energy of these small NPs is high, they are often prone to higher leaching [57].

These stability results are significant since most bodies of water have either slightly acidic or neutral pH levels, and $MnO_2@q-MOF/PMS$ can be efficiently utilized to remove pollutants from these systems.

We evaluated the reusability of our $MnO_2@q$ -MOF in four consecutive runs of the degradation reaction under a similar experimental setting (Fig. S4). Mb degradation efficacies over four cycles were 100%, 100%, 98.7%, and 97.6% within 80 min of reaction, respectively. We also measured the amount of leached metal after each run using ICP/MS, and the results showed (Table S4) that low amounts of both Fe and Mn leached, and 0.504, 0.346, 0.401, and 0.238 mg/L of Mn dissolved from the $MnO_2@q$ -MOF in four cycles, respectively, suggesting excellent stability, reusability, and efficiency of $MnO_2@q$ -MOF for PMS activation.

3.4. Mechanism of MnO₂@q-MOF/PMS system for Mb degradation

We separately studied the reaction intermediates of Mb degradation as well as PMS activation to find the underlying mechanism of the $MnO_2@q-MOF/PMS$ system for Mb degradation.

3.4.1. Determining intermediates of Mb degradation

We investigated the degradation intermediates of Mb with LC-MS/MS in the positive mode using the fraction at 30 min to detect most intermediates in the reaction pathway (Fig. S5). Based on the identified products and literature, we proposed that the Mb degradation can be divided into two possible pathways (Fig. S6) [58–61]. In the first pathway, Mb loses the chlorine group to produce Azure B (m/z 284) in the aqueous environment. A subsequent loss of two methyl groups in two consecutive stages from one of the amines produces Azure A (m/z 256) and Azure C (m/z 242), respectively. This degradation pathway can be continued by further demethylation, oxidation, and chromophore cleavage to produce intermediates with m/z 228 and 138. In a parallel

pathway, ring-opened sulfoxide intermediates (m/z 304) were detected, which originated from the interaction of the Mb with the surface of the catalyst and oxidation [61]. Subsequently, this pathway also can be continued by chromophore cleavage and smaller degradation products with m/z 123, 137, 153, 217, 206, 109. Lastly, mineralization could terminate both pathways to form SO_4^{2-} , NH_4^+ , CO_2 , and H_2O . We can conclude that the detection of hydroxylated intermediate with m/z 214, 109, and 206 suggests the mediation of ${}^{\bullet}OH$ in the system [61].

3.4.2. Identification of primary ROS generated by PMS activation

PMS can generate a diverse range of ROS such as $^{1}O_{2}$, $O_{2}^{\bullet-}$, $SO_{4}^{\bullet-}$, and $^{\bullet}OH$ [33,62,63]. To reveal the generation and the contribution of each ROS, we performed quenching experiments (Fig. 6a). We started with EtOH where the α-hydrogen can react with both $^{\bullet}OH$ ($k=1.2-2.8\times10^{9}$ $M^{-1}s^{-1}$) and $SO_{4}^{\bullet-}$ ($k=1.6-7.8\times10^{6}$ $M^{-1}s^{-1}$) followed by t-BuOH which lacks an α-hydrogen and therefore is more selective toward $^{\bullet}OH$ and react 1000 times faster with $^{\bullet}OH$ than $SO_{4}^{\bullet-}$ [64]. When 200 mM of EtOH is added no degradation inhibition of Mb was observed, however, at 2 M EtOH the reaction showed an 18% degradation inhibition. t-BuOH showed comparable results at 200 mM with no Mb degradation inhibition was observed, but at 2 M t-BuOH the inhibition was found to be 10% (Fig. S7a). These results suggest that ROS other than $SO_{4}^{\bullet-}$ and $^{\bullet}OH$ are involved in the degradation mechanism.

To further investigate the role of remaining ROS (other than $SO_4^{\bullet-}$ and ${}^{\bullet}OH$) involved in the degradation reaction, we used two different radical scavengers. First, BQ which can react with the superoxide anion radical $(O_2^{\bullet-})$ ($k=0.9-1\times10^9~\text{M}^{-1}\text{s}^{-1}$) [65], and second, His, a scavenger for singlet oxygen (${}^{1}O_2$) [33]. We observed that 30% and 32% of Mb was degraded in the presence of BQ and His, which suggests that both $O_2^{\bullet-}$ and ${}^{1}O_2$ contribute to the degradation of Mb.

To validate the quenching experiments results, we used EPR spectroscopy (Fig. 6b and c). We used DMPO as a spin trapping agent to detect $SO_4^{\bullet-}$ and ${}^{\bullet}OH$ in the form of DMPO-SO₄ or DMPO-OH adducts. In the presence of PMS alone (the control experiment), no signal was detected for either DMPO adduct, which confirms that the catalyst is responsible for the activation of PMS. The same experiment in the presence of both the catalyst and PMS resulted in a seven-line signal with an intensity ratio of 1:2:1:2:1 (hyperfine splitting constants a_N = 7.26 G, $a_{Hb} = 3.94$ G and $a_{Hc} = 3.94$ G), corresponding to the detection of 5,5-dimethyl-2-oxo-pyrrolidine-1-oxyl (DMPOX) instead of expected adducts such as DMPO-SO₄ or DMPO-OH. The DMPOX signal attenuated as the reaction progressed, suggesting that DMPO over-oxidizes in the presence of MnO2@q-MOF/PMS due to its reaction with highly active radicals such as ${}^{1}O_{2}$ and/or $O_{2}^{\bullet-}$. However, the lack of selectivity of DMPO toward SO_4^{\bullet} and ${}^{\bullet}OH$ and simultaneous reaction with $O_2^{\bullet}, {}^{1}O_2$, and ROO mean that the EPR results in water are inclusive and neither prove nor exclude the presence of SO₄^o-, and OH [66,67]. However, considering the results of LC-MS/MS and the quenching experiments, we suspect their presence in the degradation mechanism.

To further probe the ROS involved in this reaction, we performed EPR with DMPO in a methanol:water (9:1) solution using DMPO as the spin trap to trap $O_2^{\bullet-}$ (Fig. 6b). The presence of methanol in the system helps quench other radicals. The adduct signal of DMPO with $O_2^{\bullet-}$ (DMPO-OOH) was detected confirming the presence of $O_2^{\bullet-}$ in our system [68,69].

To confirm the role of $^1\mathrm{O}_2$ we used TEMP as a spin trapping agent and EPR spectroscopy. As expected, no defined EPR signal was detected from the control (PMS) solution. However, in the presence of MnO₂@q-MOF/PMS system, we detected a characteristic 3-fold peak with an intensity ratio of 1:1:1 indicative of a TEMP- $^1\mathrm{O}_2$ adduct with hyperfine splitting constant $a_N=16.89$ G (Fig. 6c). The EPR signal of the TEMPO radical persisted for more than 60 min and confirmed the role of $^1\mathrm{O}_2$ and $\mathrm{O}_2^{\bullet-}$ in the oxidation of Mb.

To explore the origin of singlet oxygen ($^{1}O_{2}$) generation and its kinetics, we performed a degradation reaction under two conditions. First, we carried out the degradation experiments in $D_{2}O$, where singlet

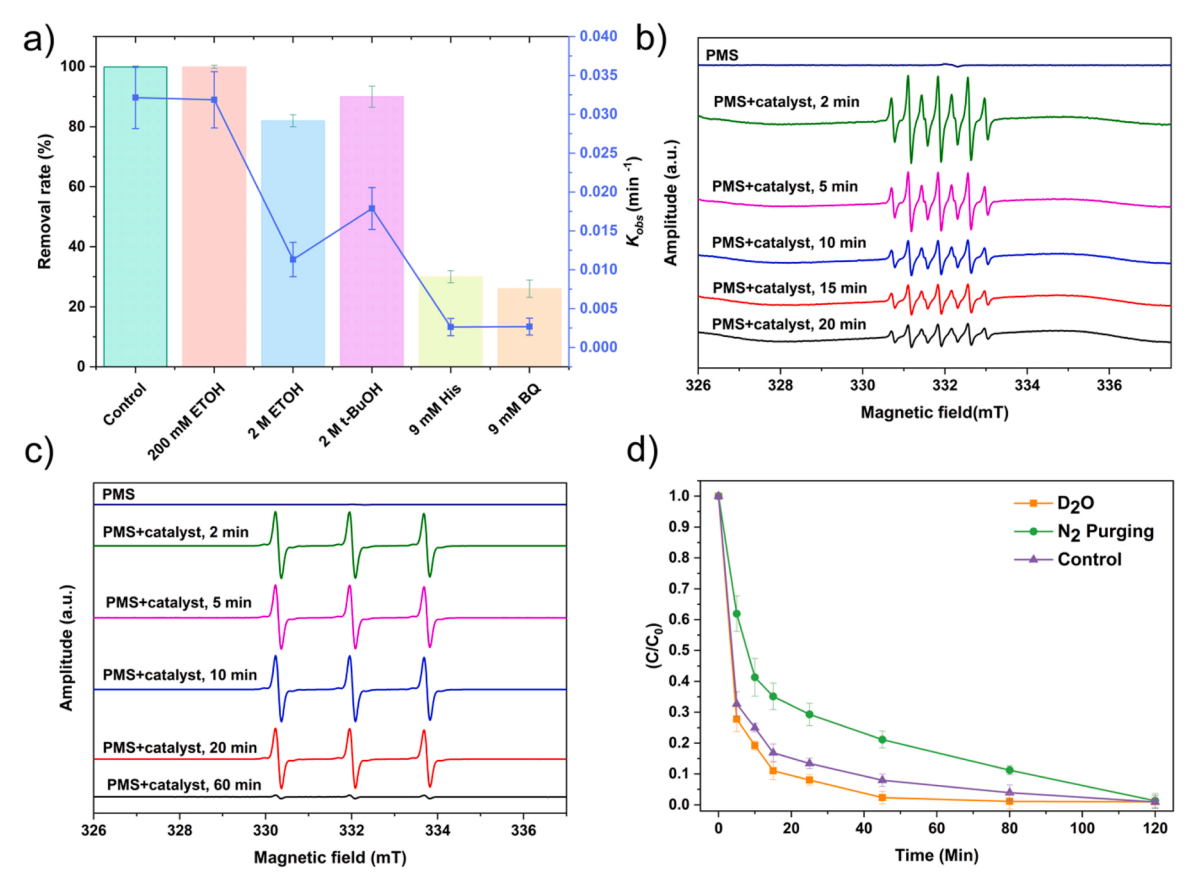


Fig. 6. a) effect of scavengers on oxidation of Mb, b) EPR spectra with DMPO, c) EPR spectra with TEMP, and d) effect of D_2O and nitrogen purging, Degradation condition: [Mb] = 50 mg/L, [PMS] = 2 mM, $[MnO_2 @q-MOF] = 0.2 \text{ g/L}$.

oxygen lifetime is higher than its lifetime in H_2O [33]. Second, we carried out an experiment while purging N_2 through the system one hour prior to adding the catalyst and PMS. The nitrogen purge was used to eliminate any singlet oxygen that might be incidental from dissolved oxygen, the metal oxide surface, or PMS [33,70].

The experimental results in D_2O show a 6.8% (0.0322–0.0344 min⁻¹) increase in k_{app} , which clearly shows that singlet oxygen is the primary ROS in our system. In addition, the results of the experiments (Fig. 6d) in the solution carried out under nitrogen atmosphere showed a 5.3% decrease in k_{app} (0.0322–0.0304 min⁻¹), compared to the control (no N_2 purge). Despite the slight decrease in the reaction rate, we can conclude that the singlet oxygen primarily originates from PMS in the presence of the MnO₂@q-MOF. Further, this experiment was conducted at pH 7, which excludes the possibility of PMS self-dissociating to singlet oxygen ($k=0.2~{\rm M}^{-1}~{\rm s}^{-1}$) as has been observed in basic environments [6].

3.4.3. Possible mechanism for Mb degradation by the $MnO_2@q\text{-MOF/PMS}$ system

To uncover the underlying reaction mechanisms for the $MnO_2@q-MOF/PMS$ catalytic system, we first excluded the contribution of leached metal ion in the activation of PMS for Mb degradation. To do that, we set up control experiments which only included 0.504 mg/L of Mn (II) and 0.678 mg/L of Fe (III) in the presence of 2 mM PMS. We chose these concentrations based on the concentrations of leached metal ions detected using ICP/MS. The control experiments indicate that 25% of Mb degradation in the presence of Mn (II) and Fe (III) ions and PMS (Fig. S7b), revealing the contribution of free leached ions to the PMS activation. The low concentration of free metal ions detected confirm that the $MnO_2@q-MOF/PMS$ system is a heterogeneous catalyst and the activation of PMS happened on the surface of the catalyst.

We then used high-resolution XPS to identify the contribution of Mn

and Fe to the functional sites on the MnO₂@q-MOF surface. The nature and contribution of each metal ion to the activity of the catalyst were compared before and after the degradation reaction. The spectra of the fresh MnO₂@q-MOF showed that Mn is present in the catalyst in three different oxidation states: Mn (II); Mn (III) and Mn (IV). After reaction, however, the deconvoluted spectra of Mn 2p (Fig. S8b and d) of MnO₂@q-MOF indicated an increase in the amount of Mn (IV) ions and a decrease in the amount of Mn (II) and Mn (III) ions. Further, the ratio of Mn (II): Mn (III): Mn (IV) which was 3:9:5 in the fresh catalyst changed to 1:3:7 after reaction, providing further evidence that PMS activation is a result of a redox-mediated process (Table S5). In addition, the Fe 2p spectra reveal the presence of Fe (II) and Fe (III) in both fresh and used catalysts (Fig. S8a and c) and the ratio of Fe (II) and Fe (III) remained almost the same. The minimal contribution of Fe to PMS activation can be attributed to the redox potential of Fe (III)/Fe (II) (0.77 eV), which makes the conversion of Fe (III) to Fe (II) by PMS thermodynamically unfavorable. The reduction potential of Fe (III)/Fe (II) is lower than that of $HSO_5^-/SO_4^{\bullet -}$ (2.5 -3.1 V) and $HSO_5^-/SO_5^{\bullet -}$ (1.1 V) [31]. In addition, it has been suggested that the transfer of electrons from Fe (II) to Mn (IV) is not thermodynamically favored [31].

The minimal variation in the ratio of Fe (II)/Fe (III) indicates a low possibility of electron transfer between Mn and Fe (Table S5). Fe could operate as a reservoir for hydroxyl ions bound to the surface of the catalyst that Mn can borrow and then facilitate activation of PMS [31]. This transfer of hydroxyl ions between Fe and Mn is crucial for PMS adsorption and activation. Hydroxyl ions adsorbed onto the catalyst surface provide substitution sites for PMS on the catalyst surface through an ion exchange process: the more hydroxyl ions, the more PMS is adsorbed [31,71,72].

Considering our results from the determination of the most prevalent ROS species, we propose that $^{1}\mathrm{O}_{2}$ formation may arise from the

recombination, or direct oxidation of $O_2^{\bullet-}$ intermediates formed on the manganese dioxide (Eqs. 1–3), and Mn (III) and Mn (II) are the functional catalytic sites for PMS activation. The mutual presence of singlet oxygen and superoxide has been detected in previous studies, where they showed that superoxide radical and singlet oxygen are the main ROS generated form PMS activation [65,73–75].

We believe that the mechanism for our catalytic system involves first the adsorption of PMS onto the surface of the catalyst, subsequently, Mn (III) and Mn (II) activate the HSO_5^- through electron transfer to produce $O_2^{\bullet-}$ which then combines with water to form 1O_2 which ultimately degrades Mb. 1O_2 has a high affinity toward electron-rich compounds with unsaturated bonds like Mb, as well as heteroatoms in the structure of electron-rich organic compounds allowing it to degrade organic compounds effectively. Mn (IV) produced from this process could then reduce to Mn (III) by HSO_5^- and regenerate the catalyst.

$$Mn(III)/Mn(II) + 2HSO_5^- \rightarrow Mn(IV)/Mn(III) + O_2^{\bullet -} + 2HSO_4^-$$
 (1)

$$2O_2^{\bullet -} + 2H_2O \to {}^1O_2 + H_2O_2 + 2OH^-$$
 (2)

$$O_2 \rightarrow {}^1O_2 \tag{3}$$

We found this mechanism to be in agreement with the finding of Fan et al., who also suggested the involvement of superoxide anion as an intermediate in the generation of singlet oxygen in a Mn(II) doped g- C_3N_4 /PMS system [65].

3.5. General applicability of MnO₂@q-MOF

HEPES, a widely used Good's buffer in the pharmaceutical industry due to its superior biocompatibility and buffering capabilities. The everincreasing use of HEPES in the industry (projected global market growth from 52 million USD in 2020–70 million USD by 2026) [76], and lack of enough study on toxicity and fate of HEPES in the aquatic environment motivated us to study its degradation. As such, we chose HEPES as a second model contaminant to demonstrate the general applicability of the catalyst. For the first time, we demonstrated the catalytic degradation of HEPES at 25 $^{\rm o}$ C at pH 7. We meticulously followed the

degradation kinetics and reaction intermediates using LC-MS/MS technique, but the degradation rate was very fast, and we were unable to measure any kinetic data accurately. Based on the degradation intermediates detected by LC-MS/MS (Fig. S9), however, we proposed a mechanism which include three major pathways for HEPES degradation (Fig. 7). In the first pathway, successive cleavage of the side chains of HEPES results in the generation of intermediates with m/z 222 and 194, respectively. In the second pathway, the piperazine ring breakage produces two intermediates with m/z 226 and 182. In the last and third pathway, we detected the n-oxide and hydroxylated derivatives of piperazine rings with m/z 255 and 271. The degradation of these intermediates to mineralization produces SO₄²⁻, NH₄⁺, CO₂ and H₂O. Our results validate developing a low-cost, sustainable, and high-efficiency system for organic micropollutants degradation. Although promising, more studies on the kinetics of the degradation mechanism and products are necessary for the further development of such systems.

3.6. Effect of environmental conditions

Unlike the controlled conditions of the reaction environment in the lab, natural polluted water sources contain a mixture of various anions that can have inhibitory effects on advanced oxidation processes (AOP) by consuming generated radicals and resulting in lower catalytic efficiency [63,77,78]. Therefore, we simulated such conditions by introducing four different anions to the reaction mixture and studied their effects on the Mb degradation in the presence of our $MnO_2@q-MOF/PMS$ system.

To start, we replaced the Milli-Q water with tap water to study the effect of naturally occurring ions in the potable water and compare it to the control experiments using deionized water (Fig. 8a). Our results showed that the Mb degradation rate (Table S6) is slower in tap water than in deionized water and the rate constant (k_{app}) reduced from 0.0322 to 0.0173 min⁻¹, which is expected due to the inhibitory impact of different ions on PMS activation or consumption of ROS [33].

We chose chloride ion (Cl⁻) as the first and most ubiquitous anion present in aqueous-based environments to study [33,79]. The measured concentration of this ion can be as high as 21 mM in groundwater [79].

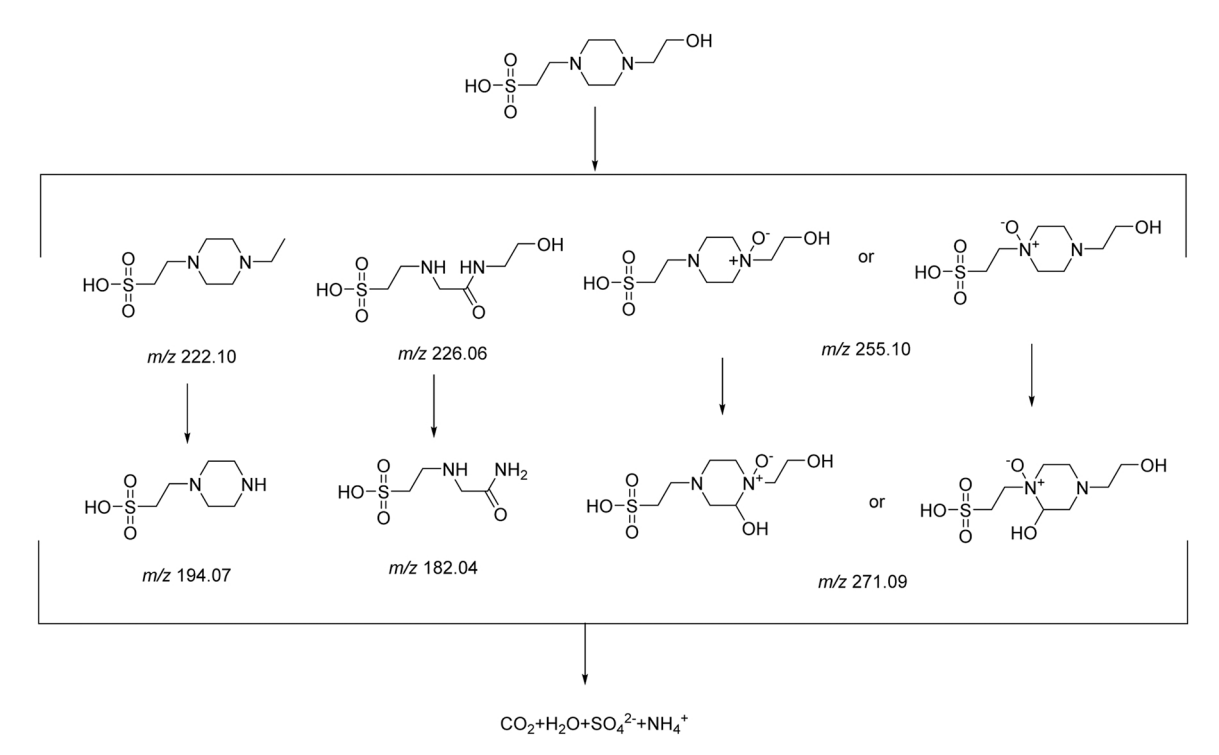


Fig. 7. Proposed HEPES degradation pathways based on LC-MS/MS results.

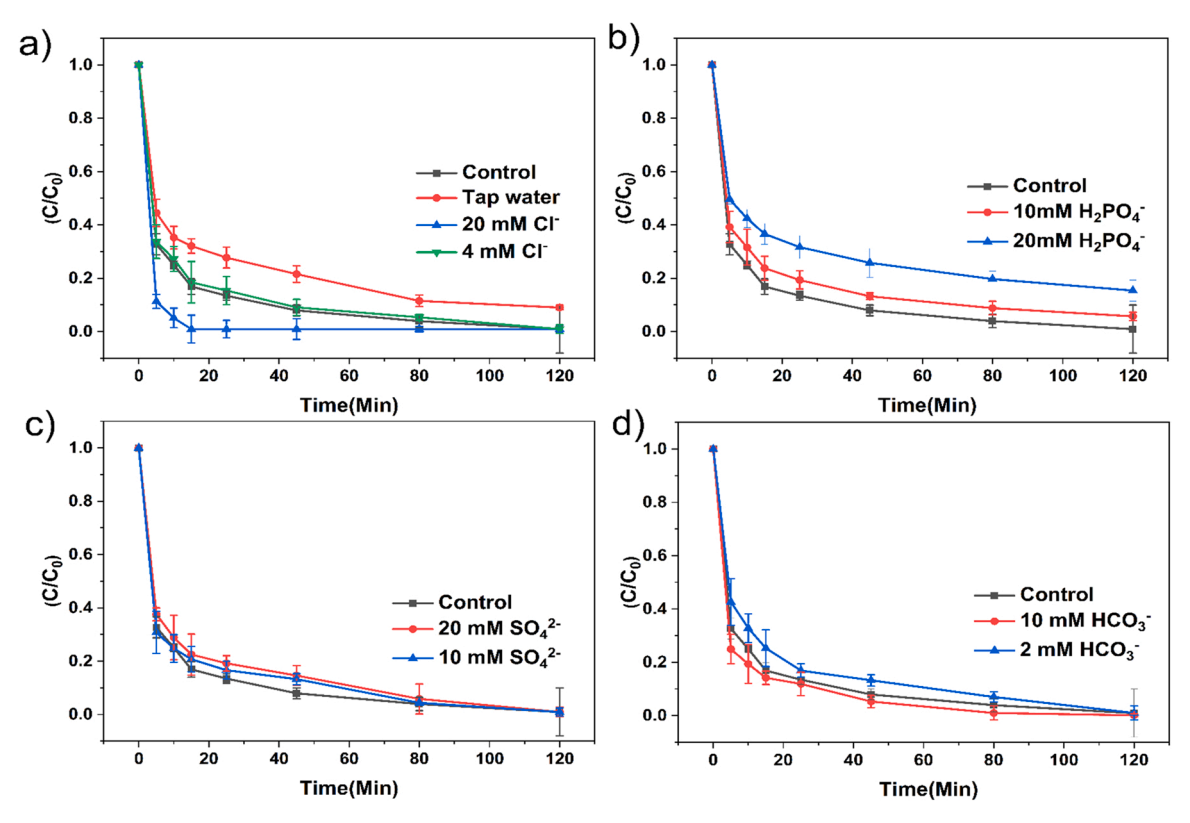


Fig. 8. Effect of a) Cl^- and tap water, b) $H_2PO_4^-$, c) SO_4^{2-} , and d) HCO_3^- on oxidation of Mb, Degradation condition: [Mb] = 50 mg/L, [PMS] = 2 mM, $[MnO_2@q-MOF] = 0.2 \text{ g/L}$.

The Cl $^-$ concentration is dependent upon radical scavenging activity such that after a critical concentration, it can act as a degrading compound by generating active chlorine radicals [79]. Our measured degradation kinetics indicated similar behavior (Fig. 8a). When we utilized 4 mM Cl $^-$ in our reaction system, we observed a minimal inhibitory effect in the reaction rate and reduced k_{app} of Mb oxidation to 0.0316 min $^{-1}$. At a higher concentration of 20 mM, the generation of chlorine radical species (Cl $^{\bullet}_2$) resulted in a rapid 96% degradation of Mb within 15 min, and k_{app} reached 0.0444 min $^{-1}$. We attribute these rapid degradation kinetics to direct oxidation of chloride by PMS and the formation of Cl $^{\bullet}_2$ as highly reactive chlorine species [79]. The potential mechanism of reactive chlorine species production are as follows [80, 81] (Eqs. 4–7):

$$2Cl^{-} + HSO_{5}^{-} + H^{+} \rightarrow SO_{4}^{2-} + Cl_{2} + H_{2}O$$
(4)

$$Cl^{-} + HSO_{5}^{-} \rightarrow SO_{4}^{2-} + HOCl$$
 (5)

$$2Cl^{-} + SO_4^{\bullet -} \rightarrow SO_4^{2-} + 2Cl^{\bullet}$$
 (6)

$$Cl^{-} + Cl^{\bullet} \rightarrow Cl_{2}^{\bullet -} \tag{7}$$

Phosphate anion $(H_2PO_4^-)$ is another commonly found anion in wastewater and is known to have an inhibitory effect on PMS/catalyst systems by quenching reactive radicals and generating weaker $H_2PO_4^+$ or $H_2PO_4^+$ radicals [82] and $H_2PO_4^-$ can also bind to the catalyst's active sites, preventing PMS activation [83]. We found that increasing the $H_2PO_4^-$ concentration from 10 mM to 20 mM, resulted in a cumulative inhibitory impact and a sharp decrease in k_{app} from 0.0191 to 0.0119 min⁻¹ (Fig. 8b). Sulfate anion (SO_4^{2-}), however, showed almost no suppression on Mb oxidation rate (Fig. 8c). The rate constants (k_{app}) for 10 and 20 mM SO_4^{2-} were 0.0320 and 0.0321 min⁻¹, respectively, comparable to the control experiment (0.0322 min⁻¹).

Bicarbonate (HCO_3^-) anion is the second most commonly found after Cl^- in natural bodies of water, with concentrations ranging from 50 to

200 mg/L [84]. We observed a slight decrease in k_{app} (0.0316 min⁻¹) when HCO $_3$ concentration was between 0 and 2 mM (Fig. 8d). However, we observed an increase in k_{app} (0.0499 min⁻¹) with increasing the bicarbonate concentration to 10 mM. We think this increase in reaction rate is due to the buffering effect of HCO $_3$ and an increase in the pH solution, which may lead to self-decomposition of PMS [79,85,86]. Some of the observations in the literature are not consistent with our results, and a few researchers reported an inhibitory effect of HCO $_3$ on the reaction rate by radical consumption [63,87]. In our system the buffering properties of HCO $_3$ is advantageous because our reaction rate is faster at higher pH levels.

4. Conclusions

We fabricated a novel quasi-MOF catalyst, MnO2@q-MOF, using an inexpensive MOF, MIL-53 (Fe), through in situ reduction of KMnO₄ to MnO₂. Further, we partially eliminated some of the phthalate linkers from the MIL-53 (Fe) base structure by using a controlled thermal treatment, providing more available sites to interact with MnO₂ inside the pores. We evaluated the performance of our catalyst by degradation of Mb in various conditions such as catalyst dosages, PMS concentrations, KMnO4 concentrations, and pH levels. We also showed that our catalyst preserved its performance after even 4 usage cycles without substantial activity loss. Using both chemical probes as radical scavengers and EPR, we found that the ¹O₂ is the dominant radical responsible for degradation. Last, we studied the effect of most found anions in wastewater, including Cl⁻, HCO₃, SO₄², and H₂PO₄⁻on our catalyst performance. We showed that Cl⁻ and HCO₃ improve the degradation rate at higher concentrations while H₂PO₄ only showed an inhibitory effect at all concentrations and SO_4^{2-} demonstrated almost no effect on our system. Finally, we used our developed MnO₂@q-MOF/PMS system for the degradation of HEPES at 25 °C and pH 7 as a proof-of-concept of broad applicability of our catalyst. Our results validated the potential of a low energy input, non-hazardous, efficient, and reusable wastewater

treatment method for eliminating organic micropollutants.

CRediT authorship contribution statement

Anahita Khojastegi: Conceptualization, Investigation, Methodology, Data curation, Writing - original draft, Writing - review & editing. Amir Mokhtare: Data curation, Investigation, Writing - review & editing. Imann Mosleh: Investigation, Writing - review & editing. Alireza Abbaspourrad: Conceptualization, Supervision, Funding acquisition, Resources, Writing - review & editing.

Declaration of Competing Interest

The authors declare that they have no known competing financial interests or personal relationships that could have appeared to influence the work reported in this paper.

Data Availability

Data will be made available on request.

Acknowledgments

This study utilized shared facilities of the Cornell Center for Materials Research sponsored through the NSF MRSEC program (DMR-1719875). This work made use of the ACERT center facilities at Cornell University, NIH/NIGMS ACERT center grant P41GM103521.

Appendix A. Supporting information

Supplementary data associated with this article can be found in the online version at doi:10.1016/j.apcata.2022.118883.

References

- [1] R.M. Burgess, K.T. Ho, M.D. Tagliabue, A. Kuhn, R. Comeleo, P. Comeleo, G. Modica, G.E. Morrison, Mar. Pollut. Bull. 30 (1995) 524-535.
- [2] D.P. Mohapatra, S.K. Brar, R.D. Tyagi, P. Picard, R.Y. Surampalli, Sci. Total Environ. 470 (2014) 58-75.
- [3] A. Gogoi, P. Mazumder, V.K. Tyagi, G.G. Tushara Chaminda, A.K. An, M. Kumar, Groundw. Sustain. Dev. 6 (2018) 169-180.
- [4] Y. Deng, R. Zhao, Curr. Pollut. Rep. 1 (2015) 167-176.
- [5] M. Salimi, A. Esrafili, M. Gholami, A. Jonidi Jafari, R. Rezaei Kalantary, M. Farzadkia, M. Kermani, H.R. Sobhi, Environ. Monit. Assess. 189 (2017) 414.
- [6] F. Ghanbari, M. Moradi, Chem. Eng. J. 310 (2017) 41-62.
- [7] S. Giannakis, K.-Y.A. Lin, F. Ghanbari, Chem. Eng. J. 406 (2020), 127083.
- [8] Z. Xiong, Y. Jiang, Z. Wu, G. Yao, B. Lai, Chem. Eng. J. 421 (2020), 127863.
- [9] J. Wang, B., H. asaer, M. Yang, R. Liu, C. Hu, H. Liu, J. Qu, Sci. Total Environ. 713 (2020), 136530.
- [10] J. Li, M. Xu, G. Yao, B. Lai, Chem. Eng. J. 348 (2018) 1012–1024.
- [11] R.J. Kalbasi, A. Khojastegi, Catal. Lett. 148 (2018) 958-971.
- [12] J. Yu, J. Cao, Z. Yang, W. Xiong, Z. Xu, P. Song, M. Jia, S. Sun, Y. Zhang, J. Zhu, J. Colloid Interface Sci. 580 (2020) 470-479.
- [13] T. Yang, D. Yu, D. Wang, T. Yang, Z. Li, M. Wu, M. Petru, J. Crittenden, Appl. Catal. B 286 (2021), 119859.
- [14] O.M. Yaghi, M.J. Kalmutzki, C.S. Diercks, Introduction to Reticular Chemistry: Metal-Organic Frameworks and Covalent Organic Frameworks, John Wiley & Sons, 2019.
- N. Stock, S. Biswas, Chem. Rev. 112 (2012) 933-969. **[15]**
- [16] Ü. Kökçam-Demir, A. Goldman, L. Esrafili, M. Gharib, A. Morsali, O. Weingart, C. Janiak, Chem. Soc. Rev. 49 (2020) 2751-2798.
- [17] G. Zhan, H.C. Zeng, Coord Rev. 320 (2016) 181-192.
- [18] X. Li, Z. Zhang, W. Xiao, S. Deng, C. Chen, N. Zhang, J. Mater. Chem. A 7 (2019) 14504-14509.
- [19] L. Chen, X. Chen, H. Liu, Y. Li, Small 11 (2015) 2642-2648.
- [20] W. Zhang, G. Lu, C. Cui, Y. Liu, S. Li, W. Yan, C. Xing, Y.R. Chi, Y. Yang, F. Huo, Adv. Mater. 26 (2014) 4056-4060.
- [21] Y.-Y. Zhang, M.-L. Zhou, Y.-S. Bao, M. Yang, Y.-H. Cui, D.-L. Liu, Q. Wu, L. Liu, Z.-B. Han, Mol. Catal, 518 (2022), 112068.
- [22] N. Tsumori, L. Chen, Q. Wang, Q.-L. Zhu, M. Kitta, Q. Xu, Chem 4 (2018) 845–856.
- [23] P. Dong, H. Wang, W. Liu, S. Wang, Y. Wang, J. Zhang, F. Lin, Y. Wang, C. Zhao, X. Duan, S. Wang, H. Sun, J. Hazard. Mater. 401 (2021), 123423.
- Γ241 Y. Cheng, X. Xiao, X. Guo, H. Yao, H. Pang, A.C.S. Sustain, Chem. Eng. 8 (2020) 8675-8680.

- [25] H. Yue, Z. Shi, Q. Wang, Z. Cao, H. Dong, Y. Qiao, Y. Yin, S. Yang, ACS Appl. Mater. Interfaces 6 (2014) 17067-17074.
- [26] H. Zhang, X. Liu, Y. Wu, C. Guan, A.K. Cheetham, J. Wang, Chem. Commun. 54 (2018) 5268-5288.
- [27] B. Liu, W. Han, X. Li, L. Li, H. Tang, C. Lu, Y. Li, X. Li, Appl. Catal. B 257 (2019), 117939.
- [28] R. Wang, L. Gu, J. Zhou, X. Liu, F. Teng, C. Li, Y. Shen, Y. Yuan, Adv. Mater. Interfaces 2 (2015) 1500037.
- [29] J. Hou, Z. Wang, P. Chen, V. Chen, A.K. Cheetham, L. Wang, Angew. Chem. Int. 59 (2020) 19434–19449.
- [30] C. Zhang, L. Ai, J. Jiang, J. Mater. Chem. A Mater. Energy Sustain. 3 (2015) 3074-3081
- [31] G.-X. Huang, C.-Y. Wang, C.-W. Yang, P.-C. Guo, H.-Q. Yu, Environ. Sci. Technol. 51 (2017) 12611-12618.
- [32] J. Du, J. Bao, Y. Liu, S.H. Kim, D.D. Dionysiou, Chem. Eng. J. 376 (2019), 119193.
- [33] J.-C.E. Yang, Y. Lin, H.-H. Peng, B. Yuan, D.D. Dionysiou, X.-D. Huang, D.-D. Zhang, M.-L. Fu, Appl. Catal. B 268 (2020), 118549.
- [34] A.J. Howarth, A.W. Peters, N.A. Vermeulen, T.C. Wang, J.T. Hupp, O.K. Farha, Chem. Mater. 29 (2017) 26-39.
- [35] M. Hossien Saghi, B. Chabot, S. Rezania, M. Sillanpää, A. Akbar Mohammadi, M. Shams, A. Alahabadi, Sep. Purif. Technol. 270 (2021), 118645.
- [36] H. Chen, Y. Liu, T. Cai, W. Dong, L. Tang, X. Xia, L. Wang, T. Li, ACS Appl. Mater. Interfaces 11 (2019) 28791-28800.
- [37] M. Meilikhov, K. Yusenko, R.A. Fischer, Dalton Trans. 6 (2009) 600-602.
- [38] C.N. Achilles, G.W. Downs, R.T. Downs, R.V. Morris, E.B. Rampe, D.W. Ming, S.J. Chipera, D.F. Blake, D.T. Vaniman, T.F. Bristow, A.S. Yen, S.M. Morrison, A.H. Treiman, P.I. Craig, R.M. Hazen, V.M. Tu, N. Castle, Amorphous Phase Characterization Through X-Ray Diffraction Profile Modeling: Implications for Amorphous Phases in Gale Crater Rocks and Soils, 2018.
- [39] V. Venuti, R. Stancanelli, G. Acri, V. Crupi, G. Paladini, B. Testagrossa S. Tommasini, C.A. Ventura, D. Majolino, J. Mol. Struct. 1146 (2017) 512–521.
- [40] Y. Qi, Y. Luan, X. Peng, M. Yang, J. Hou, G. Wang, Eur. J. Inorg. Chem. 2015 (2015) 5099–5105.
- [41] V.-P. Dinh, N.-C. Le, T.-P.-T. Nguyen, N.-T. Nguyen, J. Chem. 2016 (2016) 1-9.
- [42] N. Thomas, D.D. Dionysiou, S.C. Pillai, J. Hazard. Mater. 404 (2021), 124082.
- [43] L. Oar-Arteta, T. Wezendonk, X. Sun, F. Kapteijn, J. Gascon, Mater. Chem. Front. 1 (2017) 1709-1745.
- [44] Z. Liang, R. Zhao, T. Qiu, R. Zou, Q. Xu, EnergyChem 1 (2019), 100001.
- [45] Y.Z. Zhang, T. Cheng, Y. Wang, W.Y. Lai, Adv. Matter 28 (2016) 5242–5248.
- [46] M. Cao, Z. Zhuang, Y. Liu, Z. Zhang, J. Xuan, Q. Zhang, W. Wang, J. Colloid Interface Sci. 608 (2022) 2779–2790.
- [47] B. Yang, Z. Tian, B. Wang, Z. Sun, L. Zhang, Y. Guo, H. Li, S. Yan, R.S.C. Adv 5 (2015) 20674-20683
- [48] R.J. Kalbasi, A. Khojastegi, ChemistrySelect 3 (2018) 12666-12675.
- [49] W. Wang, W. Zhou, W. Li, X. Xiong, Y. Wang, K. Cheng, J. Kang, Q. Zhang, Y. Wang, Appl. Catal. B 276 (2020), 119142.
- [50] X. Long, S. Yang, X. Qiu, D. Ding, C. Feng, R. Chen, Jihua Tan, X. Wang, N. Chen, Q. Lei, Chem. Eng. J. 404 (2021), 127052.
- [51] K.J. Laidler, J. Chem. Educ. 61 (1984) 494.[52] R.G. Pearson, J.Chem Educ 45 (1968) 643.
- [53] S.K. Ghosh, Metal-Organic Frameworks (MOFs) for Environmental Applications, Elsevier, 2019.
- [54] G. Chen, L.-C. Nengzi, B. Li, Y. Gao, G. Zhu, X. Cheng, Sci. Total Environ. 695 (2019), 133963.
- [55] L. Hou, X. Li, Q. Yang, F. Chen, S. Wang, Y. Ma, Y. Wu, X. Zhu, X. Huang, D. Wang, Sci. Total Environ. 663 (2019) 453-464.
- [56] J. Juan-Alcañiz, J. Gascon, F. Kapteijn, J. Mater. Chem. 22 (2012) 10102-10118.
- [57] L.D. Pachón, G. Rothenberg, Appl. Organomet. Chem. 22 (2008) 288–299.
- [58] T.B. Nguyen, R.-A. Doong, C.P. Huang, C.-W. Chen, C.-D. Dong, Sci. Total Environ. 675 (2019) 531-541.
- [59] D.P. DePuccio, P. Botella, B. O'Rourke, C.C. Landry, ACS Appl. Mater. Interfaces 7 (2015) 1987-1996
- [60] C. Ma, S. Feng, J. Zhou, R. Chen, Y. Wei, H. Liu, S. Wang, Appl. Catal. B 259 (2019), 118015.
- [61] L. Wolski, M. Ziolek, Appl. Catal. B 224 (2018) 634-647.
- [62] W. Du, Q. Zhang, Y. Shang, W. Wang, Q. Li, Q. Yue, B. Gao, X. Xu, Appl. Catal. B 262 (2020), 118302.
- [63] S. Guo, H. Wang, W. Yang, H. Fida, L. You, K. Zhou, Appl. Catal. B 262 (2020), 118250.
- [64] W. Ma, N. Wang, Y. Du, P. Xu, B. Sun, L. Zhang, K.-Y.A. Lin, ACS Sustain. Chem. Eng. 7 (2019) 2718-2727.
- [65] J. Fan, H. Qin, S. Jiang, Chem. Eng. J. 359 (2019) 723-732.
- [66] J. Liu, F. An, C. Zhu, D. Zhou, Sci. Total Environ. 759 (2021), 142864.
- [67] S. Zhu, X. Li, J. Kang, X. Duan, S. Wang, Environ. Sci. Technol. 53 (2019) 307-315.
- [68] C. Tan, Q. Xu, T. Sheng, X. Cui, Z. Wu, H. Gao, H. Li, J. Hazard. Mater. 398 (2020), 123084.
- [69] W. Li, Y. Wu, Y. Gao, S. Xing, Res. Chem. Intermed. 45 (2019) 5549-5558.
- [70] H. Li, C. Shan, B. Pan, Environ. Sci. Technol. 52 (2018) 2197-2205.
- [71] H. Tamura, K. Mita, A. Tanaka, M. Ito, J. Colloid Interface Sci. 243 (2001) 202-207.
- [72] H. Tamura, A. Tanaka, K. Mita, R. Furuichi, J. Colloid Interface Sci. 209 (1999)
- [73] Y. Wang, D. Cao, M. Liu, X. Zhao, Catal. Commun. 102 (2017) 85-88.
- S. Yang, P. Wu, J. Liu, M. Chen, Z. Ahmed, N. Zhu, Chem. Eng. J. 350 (2018)

- [75] F. Guo, K. Wang, J. Lu, J. Chen, X. Dong, D. Xia, A. Zhang, Q. Wang, Chemosphere 218 (2019) 1071–1081.
- [76] https://www.theexpresswire.com/pressrelease/HEPES-Market-Size-In-2022-isestimated-to-grow-at-a-modest-CAGR-of-more-than-52-During-the-forecast-period-2022-2026-with-Top-Countries-Data-In-depth-145-Pages-Report_15429928 (accessed February 19, 2022).
- [77] C. Tan, N. Gao, D. Fu, J. Deng, L. Deng, Sep. Purif. Technol. 175 (2017) 47–57.
 [78] Y. Feng, D. Wu, Y. Deng, T. Zhang, K. Shih, Environ. Sci. Technol. 50 (2016) 3119-3127.
- [79] H. Lin, S. Li, B. Deng, W. Tan, R. Li, Y. Xu, H. Zhang, Chem. Eng. J. 364 (2019) 541-551.
- [80] J. Wang, S. Wang, Chem. Eng. J. 411 (2021), 128392.
- [81] J. Wang, S. Wang, Chem. Eng. J. 334 (2018) 1502-1517.
- [82] Y. Xu, H. Lin, Y. Li, H. Zhang, Sci. Total Environ. 609 (2017) 644-654.
- [83] Y. Xu, J. Ai, H. Zhang, J. Hazard. Mater. 309 (2016) 87-96.
- [84] Q.-H. Zhang, P.-A. Sun, S.-Y. He, H. Wen, M.-L. Liu, S. Yu, Huan Jing Ke Xue 39 (2018) 1065–1075.
- [85] M. Wang, Y. Cui, H. Cao, P. Wei, C. Chen, X. Li, J. Xu, G. Sheng, Appl. Catal. B Environ. 282 (2021), 119585.
- [86] J. Wang, S. Wang, Chem. Eng. J. 401 (2020), 126158.
- [87] Y. Wang, D. Cao, X. Zhao, Chem. Eng. J. 328 (2017) 1112–1121.